Solar Energy Materials & Solar Cells 121 (2014) 80–84

Contents lists available at ScienceDirect

Solar Energy Materials & Solar Cells

journal homepage: www.elsevier.com/locate/solmat

Hole transit in P3HT:PCBM solar cells with embedded gold nanoparticles

Cheng-En Cheng [a,b], Zingway Pei [c], Chia-Chen Hsu [d], Chen-Shiung Chang [a], Forest Shih-Sen Chien [b,e,*]

[a] Department of Photonics and Institute of Electro-Optical Engineering, National Chiao Tung University, Hsinchu, Taiwan
[b] Department of Applied Physics, Tunghai University, Taichung, Taiwan
[c] Graduate Institute of Optoelectronic Engineering, Department of Electrical Engineering, National Chung Hsin University, Taichung, Taiwan
[d] Department of Physics, National Chung Cheng University, Chiayi, Taiwan
[e] Tunghai Green Energy Development and Management Institute, Tunghai University, Taichung, Taiwan

ARTICLE INFO

Article history:
Received 10 June 2013
Received in revised form
20 September 2013
Accepted 21 October 2013
Available online 21 November 2013

Keywords:
Polymer solar cells
Gold nanoparticles
Hole transit
Impedance spectroscopy

ABSTRACT

The electrical properties of polymer solar cells (PSCs) with gold nanoparticles (AuNPs) embedded in the hole transport layers (HTLs) were investigated. The PSCs with AuNP-embedded HTLs exhibited 8%, 9.5%, and 22% enhancement in short-circuit current density, open-circuit voltage, and power conversion efficiency, respectively. The low contact resistance at the active layer/HTL interface resulted in the high collection efficiency and low electron–hole recombination. The downshift of the Fermi energy in AuNP-embedded HTLs lowered the energy barrier and thinned the depletion layer at the active layer/HTL interface, accounting for the enhanced collection efficiency.

1. Introduction

Polymer solar cells (PSCs) have attracted considerable attention because of their desirable features (e.g., manufacturing simplicity, low cost, light weight, and mechanical flexibility) [1–3]. Recently, PSCs with bulk heterojunction (BHJ) structures have been widely studied, regarding the increase of the interfacial area of the donor/acceptor to improve the efficiency of electron–hole pair dissociation [4]. Studies have demonstrated that the power conversion efficiency (PCE) of BHJ-based PSCs approaches 6.5% [5]. However, compared with inorganic solar cells, the lower dissociation rate of electron–hole pairs and lower carrier mobility of PSC yields a relatively lower PCE. Improving the photovoltaic performance of PSCs is a critical issue for the wide deployment of PSCs.

To overcome the issue of low efficiency of PSCs, metallic nanoparticles, such as gold nanoparticles (AuNPs), have been introduced into the hole transport layers (HTLs) of poly(3,4-ethylenedioxythiophene) poly(styrenesulfonate) (PEDOT:PSS) in PSCs to improve photovoltaic performance. Several possible mechanisms have been proposed to interpret the effects of AuNPs in PSCs. For instance, the interfacial area of active layers/HTLs and the conductivity of HTLs are increased by AuNPs [6]; the excitation probability of electron–hole pairs and the dissociation rate of the pairs in PSCs are enhanced by the localized surface plasmons (LSPs) of AuNPs [7,8]. However, the influence of AuNPs embedded in HTLs on the hole transit in PSCs is unclear.

To study the role that the embedded AuNPs play in PSCs regarding hole transit, the PSCs with AuNP-embedded HTLs (AuNP-PSCs) were investigated by impedance spectroscopy (IS) and valence band photoelectron spectra (VBPES), in addition to typical photovoltaic characterizations [current density to bias voltage (J–V) and incident monochromatic photon-to-current conversion efficiency (IPCE)]. IS has been widely applied to investigate the carrier dynamics of PSCs [9,10]. Compared with the PSCs with pristine HTL (ref-PSCs), 8% and 22% relative enhancements of short-circuit current density (J_{sc}) and PCE in AuNP-PSCs were achieved, respectively. Based on the IS analysis, AuNP-PSCs presented a lower contact resistance at the active layer/HTL interface, resulting in faster hole transit and higher photocurrent. The VBPES indicated that the AuNP-embedded HTL has a lower Fermi energy (E_F), which explains the low contact resistance and enhancement of open-circuit voltage (V_{oc})

2. Experimental

The AuNP colloid was synthesized by the reduction of $HAuCl_4$ with sodium citrate [11]. The mean diameter of AuNPs was

* Corresponding author. Tel.: +886423590121; Fax: +886423594643.
E-mail address: fsschien@thu.edu.tw (F. Shih-Sen Chien).

0927-0248/$ - see front matter © 2013 Elsevier B.V. All rights reserved.
http://dx.doi.org/10.1016/j.solmat.2013.10.017

approximately 10 nm, measured by high resolution transmission electron microscopy. The AuNPs were separated from the solution by a centrifuge and were then mixed with PEDOT:PSS. The weight percentages of AuNPs in PEDOT:PSS were approximately 0.05%, 0.10%, 0.15% and 0.20%. The substrate was indium tin oxide (ITO) glass, with sheet resistance of 15 Ω/sq and transmittance $>90\%$. The substrate was treated by UV-ozone for 30 min. The PEDOT:PSS was spin-coated on ITO glass as an HTL. The solvent was expelled by thermal treatment at 140 °C for 10 min. The thickness of the HTL was 45 nm with a roughness of 2.3 nm, verified by atomic force microscopy (AFM). The corresponding areal density of the 0.15 wt% AuNPs in the HTL was approximately 10 μm^{-2}. The PEDOT:PSS-coated ITO-glass was transferred into a nitrogen-filled glove box immediately after thermal treatment. Blended solutions of poly(3-hexylthiophene) (P3HT) and 6,6-phenyl-C61-butyric acid methyl ester (PCBM) (at a weight ratio of 1:1) were prepared in 1,2-dichlorobenzene (DCB) at a concentration of 10 mg/mL. The P3HT:PCBM solution was spin-coated onto PEDOT:PSS and naturally dried in the glove box. The thickness of the P3HT:PCBM active layer was approximately 120 nm. A 100-nm thick Al cathode was deposited by thermal evaporation on the active layer with a shadow mask. A post-annealing treatment at 150 °C for 30 min in the glove box was applied to produce phase separation between P3HT and PCBM. Finally, the cells were sealed by lamella glasses. The characterizations of the *J–V*, IPCE, and complex impedance spectra (by Agilent 4284 A LCR meter) were conducted under the irradiation of an AM 1.5 G solar simulator in ambience. The VBPES was performed by a focused X-ray photoelectron spectrometer (ULVAC-PHI, PHI 500 VersaProbe) to study the variation of band energy of the HTLs. During the VBPES measurement, the charging effect was eliminated by a dual-beam charge neutralization system so that the test samples were electrically floated and the vacuum levels of each sample were considered aligned.

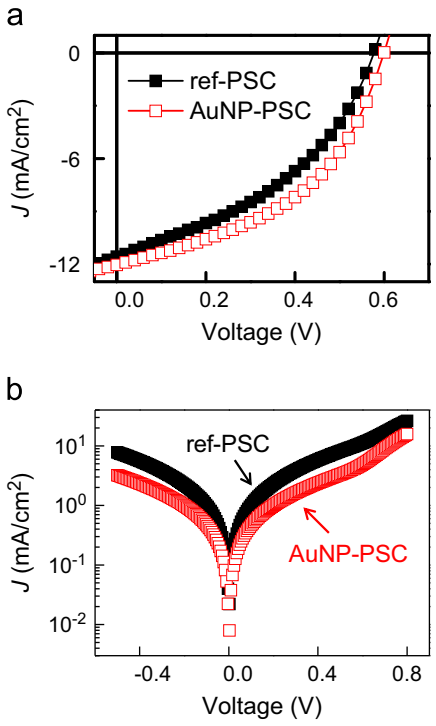

Fig. 1. *J–V* characteristics of the ref-PSC and AuNP-PSC with 0.15 wt% AuNPs in HTL (a) under illumination (AM 1.5 G), and (b) in the dark.

3. Results and discussion

Among those different weight percentages of AuNPs in the HTL, only the PSC with 0.15 wt% AuNPs exhibited enhancement in performance, and the AuNP-PSCs with other weight percentages were poorer than the ref-PSC. Fig. 1(a) shows the photo *J–V* characteristic curves of ref-PSCs and AuNP-PSCs of 0.15 wt%. These results were the average of four devices. The photovoltaic parameters and parasitism resistances of the *J–V* curves of all PSCs are summarized in Table 1. By parasitism resistance analysis, the series resistance (R_s) and shunt resistance (R_{sh}) were calculated from the *J–V* characteristic curves. In general, the parasitical R_s and R_{sh} are associated with ohmic loss and leakage resistance, respectively [12]. The R_s of the AuNP-PSCs with 0.15 wt% was lower than that of ref-PSC, but R_s of the rest AuNP-PSC was higher. We suggest that two influences appeared in the HTL due to the embedment of AuNPs. The first one is that impurities were introduced along with AuNPs, causing the decrease of conductivity. The second is the charge carriers of HTL were redistributed, because AuNPs possessed a high electron affinity and enclosed by negative charges from HTL, causing the increase of hole concentration in HTL (this consists with the downshift of E_F derived from VBPES shown later). Consequently, those two influences compete against each other. The former was dominant under 0.1 wt%, and the latter was dominant near 0.15 wt %. With a higher percentage of AuNPs ($\geq$0.2 wt%), the HTL was degraded with the embedded alien species and no enhancement of PSCs was observed. Therefore, only the PSCs with 0.15 wt% AuNPs in HTL were discussed in this study.

The ref-PSCs demonstrated J_{sc} of 11.1 mA/cm^2, V_{oc} of 546 mV, filling factor (*FF*) of 43%, and overall PCE of 2.7%. The performance of ref-PSCs is not as good as that of PSCs with LiF/Al cathodes (PCE of 3.5% [13]), but comparable with that of PSCs in similar designs (PCE of 2.1% [14] and 2.6% [12]). For the 0.15 wt% AuNP-PSCs, the corresponding photovoltaic parameters are as follow: J_{sc} of 12.1 mA/cm^2, V_{oc} of 598 mV, *FF* of 46%, and overall PCE of 3.3%. The AuNP-PSCs showed an 8% and 9.5% enhancement in J_{sc} and V_{oc}, respectively. The R_s and R_{sh} were 16 Ω m^2 and 198 Ω cm^2 for ref-PSCs, and 12 Ω cm^2 and 275 Ω cm^2 for AuNP-PSCs, respectively. The lower R_s in AuNP-PSCs was attributed to the lower contact resistance (to be discussed later with the IS results), and accounted for the enhancement of J_{sc}. The higher R_{sh} of AuNP-PSC indicates that the recombination of electron–hole pairs was suppressed, resulting in a higher V_{oc}. Fig. 1(b) shows the dark *J–V* curves of both PSCs. The

Table 1
Photovoltaic parameters and parasitism resistances (R_{sh} and R_s) of ref-PSCs and AuNP-PSCs with various weight percentage of embedded AuNPs.

Device	J_{sc} (mA/cm^2)	V_{oc} (mV)	FF (%)	PCE (%)	R_{sh} (Ω-cm^2)	R_s (Ω-cm^2)
ref-PSC	11.2	546	43	2.7	198	16
AuNP-PSC						
0.05 wt%	8.1	586	45	2.1	288	17
0.10 wt%	7.8	601	42	1.7	273	18
0.15 wt%	12.1	598	46	3.3	275	12
0.20 wt%	7.5	587	46	2.0	279	18

lower current density of AuNP-PSC was observed under a reverse bias and moderate forward bias. The lower current density implies that the AuNP-PSC exhibits a lower electron–hole recombination, which is consistent with the results of R_{sh}. The current density of the AuNP-PSC showed a higher slope in the high injection regime (bias > 0.6 V), consistent with the result of the lower R_s of AuNP-PSC.

The morphological changes of the HTLs and active layers were analyzed with a tapping-mode AFM to observe the influence of AuNPs on the roughness because the contact area varies with roughness [6]. The results of the AFM measurement showed that the HTLs exhibited surface roughness of 2.3 nm (pristine) and 2.4 nm (AuNP-embedded); the surface roughness of the active layers are 24.3 nm (on the pristine HTL) and 24.6 nm (on the AuNP-embedded HTL). The embedded AuNPs caused no substantial change in the morphology of the HTLs and active layers, indicating the enhancement in the photocurrent of AuNP-PSCs was not related with the roughness of the HTLs nor the active layers in this study.

IPCE spectroscopy was employed to characterize the optical response of both PSCs. The IPCE spectrum represents the ratio of generated electrons to incident photons at a single wavelength, and is expressed by the following equation:

$$\mathrm{IPCE}(\%) = \frac{1240 \times J_{SC}(\lambda)}{\lambda \times P_{in}(\lambda)} \times 100\%, \quad (1)$$

where $J_{sc}(\lambda)$ is the short-circuit current density at monochromatic wavelength λ in μA/cm^2, and $P_{in}(\lambda)$ is the power of incident monochromatic light in μW/cm^2. Fig. 2(a) shows the IPCE spectra of ref- and AuNP-PSCs, and Fig. 2(b) shows the relative enhancement in IPCE obtained by

$$\frac{IPCE_{AuNPs} - IPCE_{pristine}}{IPCE_{pristine}} \times 100\% \quad (2)$$

The relative enhancement (ranging from 420 to 670 nm) caused by AuNPs was approximately 5.6%, which was consistent with the enhancement of J_{sc}. Nevertheless, no remarkable enhancement related to the LSP-induced absorption was noted (i.e., a specific peak at 520 nm in relative IPCE enhancement). The nature of LSPs is a near-field phenomenon, which means the electromagnetic field of LSPs decays rapidly with the distance [15] (in few nanometers) from the dielectric/metal interface. In addition, for normal or small-angle incidence, the excited field of LSPs distributes laterally, rather than vertically into the adjacent active layer [6]. Therefore, LSPs hardly influence the photovoltaic behavior of the adjacent active layer. It might not be possible to observe the IPCE enhancement due to LSPs, even if the weight percentage of AuNPs is significantly higher than 0.15 wt%.

To further understand the influences on optical properties of HTLs and active layers caused by AuNPs, the absorbance spectra of both HTLs (pristine and AuNP-embedded) and P3HT:PCBM layers on each HTL were taken by UV–vis spectroscopy, as shown in Figs. 2(c) and 2(d). The total absorbance spectra showed no substantial difference between the HTLs and between the P3HT:PCBM layers on each HTL. Apparently, the concentration of AuNPs was too low to induce the loss of light by scattering. Based on the arguments from IPCE and absorbance spectra, we suggest that the IPCE enhancement is not attributed to the AuNP-related LSPs.

To understand the mechanism of the PCE enhancement by AuNPs, the quantum efficiencies involved in the energy conversion have to be considered. The IPCE can be expressed by

$$IPCE(\lambda) = \eta_A(\lambda) \times \eta_{ED}(\lambda) \times \eta_{CS}(\lambda) \times \eta_{CC}(\mu, \tau), \quad (3)$$

where $\eta_A(\lambda)$, $\eta_{ED}(\lambda)$, $\eta_{CS}(\lambda)$, and $\eta_{CC}(\mu,\tau)$ represent the efficiencies of absorption, exciton diffusion, charge separation, and carrier collection, respectively, and μ and τ are the carrier mobility and lifetime, respectively [16]. The absorbance spectra indicate that the embedment of AuNPs caused no change in $\eta_A(\lambda)$, $\eta_{ED}(\lambda)$, and $\eta_{CS}(\lambda)$. Hence, only $\eta_{CC}(\mu,\tau)$ was increased due to AuNPs. The increase of $\eta_{CC}(\mu,\tau)$ due to the embedment of AuNPs was studied by IS. The impedance spectra were observed under illumination without a bias. The Nyquist plots of complex impedance of both PSCs are shown in Fig. 3(a). The carrier dynamics of the diffusion–recombination processes in P3HT:PCBM solar cells can be simulated by the effective Garcia–Belmonte series model [9,17] [Fig. 3(b)]. In this model, an effective series resistance (R_0) consists of the resistance of wire contacts and bulk materials. An effective transit resistance (R_t) consists of the resistance of the carrier transit in the active layer and the resistance of the active layer/electrode interfaces. An effective recombination resistance (R_{rec}) is related to the global recombination process of electron–hole pairs in the active layer. A global capacitance of the entire cell and a diffusion capacitance at the P3HT/PCBM interface are represented by constant phase elements (CPE_s) because they are considered non-ideal capacitors that consist of non-homogeneous interpenetrating P3HT:PCBM blends. The global and diffusion capacitances are denoted as CPE_g

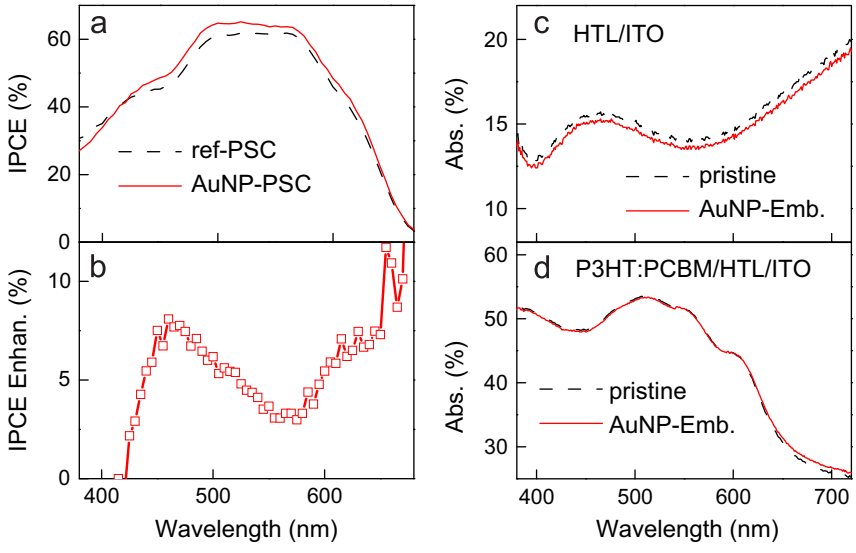

Fig. 2. (a) IPCE spectra of a ref-PSC and an AuNP-PSC and (b) relative IPCE enhancement estimated by Eq. (2). (c) Absorbance spectra of a pristine HTL and AuNP-embedded HTL, and (d) absorbance spectra of P3HT:PCBM active layers on the pristine HTL and AuNP-embedded HTL.

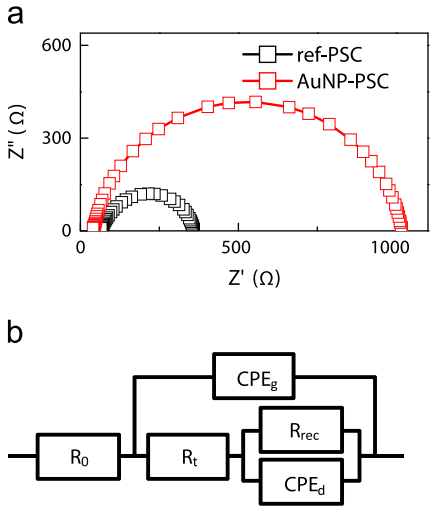

Fig. 3. (a) Nyquist plots of the complex impedance spectra of a ref-PSC and an AuNP-PSC; the spectra were simulated by (b) the effective Garcia–Belmonte series model.

Table 2
Simulated results from the impedance spectra of the ref-PSCs and AuNP-PSCs (0.15 wt%).

Device	R_0 (Ω)	R_t (Ω)	R_{rec} (Ω)	B_g[a] (nF)	B_d[a] (nF)	τ_d (μs)	μ ($cm^2V^{-1}s^{-1}$)
ref-PSC	65	80	214	92	118	9.4	0.5×10^{-3}
AuNP-PSC	37	47	935	97	17	0.8	7.0×10^{-3}

[a] B_g and B_d are the magnitude parameters of CPE$_g$ and CPE$_d$.

and CPE$_d$. The impedance of a CPE is rewritten as

$$Z_{CPE}=\frac{1}{B(i\omega)^P}, \quad (4)$$

where B and P are the magnitude and phase parameter, respectively (both are frequency-independent). P is to represent the non-homogeneous surface effects (e.g., porous and surface trap), and B_g/B_d to the magnitude of CPE$_g$/CPE$_d$. The spectra [Fig. 3(a)] were simulated by the effective Garcia–Belmonte model with the Z-view software in the frequency region of 20 Hz to 1 MHz. The simulation results are summarized in Table 2.

The simulation results showed that R_t was 79.8 Ω for the ref-PSC and 46.5 Ω for the AuNP-PSC. The R_t of AuNP-PCS was 42% lower than that of ref-PSC, indicating that R_t was improved. Since the conditions of the crystalline of P3HT fibrils [18] and the cathode/active layer contact were fixed, the improvement in R_t resulted from the decrease of the contact resistance of the active layer/HTL interface. Furthermore, the R_{rec} increased from 214 Ω (ref-PSC) to 935 Ω (AuNP-PSC), and B_d decreased from 118 nF (ref-PSC) to 17 nF (AuNP-PSC) because of the embedded AuNPs. The lower diffusion capacitance means the lower charge carrier density at the P3HT/PCBM interface, and the greater leakage resistance means the lower electron–hole recombination rate. The effective transit time (τ_d) [17] under a short-circuit condition can be obtained by

$$\tau_d = R_t \times B_d \quad (5)$$

The mobility in active layers under a short-circuit condition in the PSCs can then be estimated by the following equation [9]:

$$\mu=\frac{eL^2}{k_BT\tau_d}, \quad (6)$$

where e, L, k_B, and T represent the elementary charge, thickness of the active layer (120 nm), the Boltzmann constant, and the temperature (40 °C under illumination), respectively. Both τ_d and μ are presented in Table 2. The effective transit time was 9.4 μs for ref-PSCs and 0.8 μs for AuNP-PSCs. The carrier transit time in AuNP-PSC decreased by an order of magnitude. In addition, the mobility in a short-circuit condition was 5×10^{-4} cm^2 V^{-1} s^{-1} for the ref-PSC, and 7×10^{-3} cm^2 V^{-1} s^{-1} for the AuNP-PSC. Both the effective transit time and mobility were improved in AuNP-PSCs, indicating that the hole collection became more efficient, the electron–hole recombination was suppressed, and the photocurrent and filling factor were enhanced. Hence, the higher carrier collection efficiency in AuNP-PSCs is attributed to the lower transit resistance at the P3HT/HTL interface and diffusion capacitance at the P3HT/PCBM junction.

The mechanism to cause the decrease of R_t due to the embedded AuNPs is critical in this study. To understand this mechanism, VBPES was applied to study the variation of the band energy of the HTLs. Fig. 4(a) shows the VBPES of a pristine HTL and AuNP-embedded HTL. The results of the VBPES indicated that E_F of AuNP-embedded HTLs shows an averaged downshift of 0.16 ± 0.02 eV compared with that of pristine HTLs. The downshift of E_F can be attributed to the increase of the hole concentration due to the embedment of AuNPs, because negative charges were attracted by the high-electron-affinity AuNPs and charge carriers redistributed in the HTLs, i.e., the increase of the mobile hole concentration. The Hall measurement of HTLs reveals that the AuNP-embedded HTL has a higher

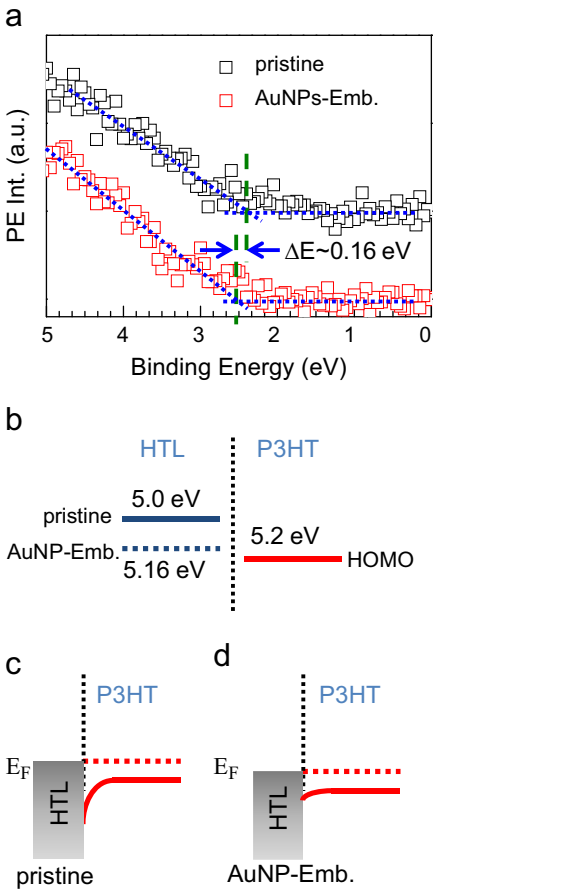

Fig. 4. (a) Valence band photoemission spectra of pristine and AuNP-embedded HTLs. Zero binding energy is referred to as the Fermi energy of the electron energy analyzer of the spectrometer. (b) Band diagram of HTLs (pristine and AuNP-embedded) and P3HT before band alignment (not to scale). Band bending at the P3HT/HTL interface (in the short-circuit condition) with pristine HTL (c) and AuNP-embedded HTL (d) in equilibrium.

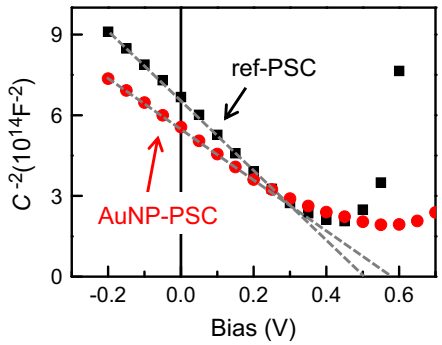

Fig. 5. Mott–Schottky curves of a ref-PSC and AuNP-PSC. The dashed straight lines (linear fitting in the bias range of −0.2 V to 0.2 V) yield the value of V_{bi} in each PSC.

hole concentration than that of pristine HTL, which supports the argument about the downshift of E_F. The energy difference between E_F of pristine HTLs and the highest occupied molecular orbital (HOMO) of P3HT was approximately 0.2 eV [19], as depicted in the band diagram of the pristine HTL and P3HT [Fig. 4(b)]. This energy difference induces a band bending at the interface, and the interface is depleted, thereby hindering the hole transit (hopping) at the interface [Fig. 4(c)]. With the embedment of AuNPs, the energy difference between the HTL and HOMO of P3HT lessens. The barrier height and the depletion width at the interface are reduced substantially [Fig. 4(d)]. Consequently, the contact resistance is reduced at the P3HT/HTL interface and the hole transit is improved, as inferred from the IS results. In addition, the downshift of AuNP-embedded HTL energy increased the energy difference between the anode and cathode. The increase in V_{oc} of the AuNP-PSCs is attributed to both the increase of R_{sh} and the downshift of the HTL energy.

Fig. 5 shows the plot of C^{-2} with bias voltage V, which were taken in the dark at a frequency of 100 Hz. The behavior of the depletion capacitance is expressed by the Mott–Schottky equation [9]

$$C^{-2} = \frac{2(V_{bi} - V)}{A^2 e \varepsilon \varepsilon_0 N_A}, \tag{7}$$

where V_{bi} is the built-in potential, A is the active area, e represents the elementary charge, ε represents the relative dielectric constant (assumed to be 3 for P3HT:PCBM [9]), ε_0 is the permittivity of vacuum, and N_A is the electron concentration of PCBM. The built-in potentials V_{bi} were extracted by the intercept of the fitted line (in the bias range of −0.2 V to 0.2 V) with the x-axis (Fig. 5), and yielded a V_{bi} of 507 mV for the ref-PSC, and 585 mV for the AuNP-PSC. The higher V_{bi} in AuNP-PSC implies a higher V_{oc}, which is consistent with the results of the VBPES.

4. Conclusion

The performance of PSCs with 10 nm AuNP-embedded HTLs was studied. The J_{sc}, V_{oc}, and PCE were enhanced by 8%, 9.5%, and 22%, respectively, due to the embedment of AuNPs. The IS analysis demonstrated that the enhanced photocurrent was caused by the improvement in the hole collection and the suppression of the electron–hole recombination, because of the lower contact resistance at the P3HT/HTL interface. The VBPES analysis indicated the energy difference between the Fermi energy of HTLs and the HOMO of P3HT was lowered because of the embedment of AuNPs in HTLs, and the barrier height and the depletion width were also reduced, leading to the lower contact resistance. The downshift in Fermi energy of HTL and the suppression of electron–hole recombination resulted in the increase of V_{oc}.

References

1 F.C. Krebs, Fabrication and processing of polymer solar cells: a review of printing and coating techniques, Sol. Energy Mater. Sol. Cells 93 (2009) 394–412.
2 F.C. Krebs, M. Jørgensen, K. Norrman, O. Hagemann, J. Alstrup, T.D. Nielsen, J. Fyenbo, K. Larsen, J. Kristensen, A complete process for production of flexible large area polymer solar cells entirely using screen printing—first public demonstration, Sol. Energy Mater. Sol. Cells 93 (2009) 422–441.
3 F.C. Kerbs, T.D. Nielsen, J. Fyenbo, M. Wadstrom, M.S. Pedersen, Manufacture, integration and demonstration of polymer solar cells in a lamp for the "Light Africa" initiative, Energy Environ. Sci 3 (2010) 512–525.
4 G. Li, V. Shrotriya, J.S. Huang, Y. Yao, T. Moriarty, K. Emery, Y. Yang, High-efficiency solution processable polymer photovoltaic cells by self-organization of polymer blends, Nat. Mater. 4 (2005) 865–868.
5 G. Zhao, Y. He, Y. Li, 6.5% efficiency of polymer solar cells based on poly(3-hexylthiophene) and indene-C_{60} bisadduct by device optimization, Adv. Mater 22 (2010) 4355–4358.
6 D.D.S. Fung, L. Qiao, W.C.H. Choy, C. Wang, W.E.I. Sha, F. Xie, S. He, Optical and electrical properties of efficiency enhanced polymer solar cells with Au nanoparticles in a PEDOT–PSS layer, J. Mater. Chem. 21 (2011) 16349–16356.
7 F.C. Chen, J.L. Wu, C.L. Lee, Y. Hong, C.H. Kuo, M.H. Huang, Plasmonic-enhanced polymer photovoltaic devices incorporating solution processable metal nanoparticles, Appl. Phys. Lett. 95 (2009) 013305.
8 J.L. Wu, F.C. Chen, Y.S. Hsiao, F.C. Chien, P. Chen, C.H. Kuo, M.H. Huang, C.S. Hsu, Surface plasmonic effects of metallic nanoparticles on the performance of polymer bulk heterojunction solar cells, ACS Nano 5 (2011) 959–967.
9 G. Garcia-Belmonte, A Munar, E.M. Barea, J. Bisquert, I. Ugarte, R. Pacios, Charge carrier mobility and lifetime of organic bulk heterojunctions analyzed by impedance spectroscopy, Org. Electron. 9 (2008) 847–851.
10 G. Garcia-Belmonte, P.P. Boix, J. Bisquert, M. Sessolo, H.J. Bolink, Simultaneous determination of carrier lifetime and electron density-of-states in P3HT:PCBM organic solar cells under illumination by impedance spectroscopy, Sol. Energy Mater. Sol. Cells 94 (2010) 366–375.
11 J.W. Slot, H.J. Geuze, A new method of preparing gold probes for multiple-labeling cytochemistry, J. Cell Biol 38 (1985) 87–93.
12 B.P. Devi, S. Thiyagu, Z. Pei, "Electrical annealing" effect in bulk heterojunction polymer solar cell, Thin Solid Film 529 (2013) 54–57.
13 F. Padinger, R.S. Rittberger, N.S. Sariciftci, Effects of postproduction treatment on plastic solar cells, Adv. Funct. Mater. 13 (2003) 85–88.
14 W.H. Baek, H. Yang, T.-S. Yoon, C.J. Kang, H.H. Lee, Y.-S. Kim, Effect of P3HT:PCBM concentration in solvent on performances of organic solar cells, Sol. Energy Mater. Sol. Cells 93 (2009) 1263–1267.
15 A.V. Zayats, I.I. Smolyaninov, A.A. Maradudin, Nano-optics of surface plasmon polaritons, Phys. Rep. 408 (2005) 131–314.
16 G. Li, R. Zhu, Y. Yang, Polymer solar cells, Nat. Photonics 6 (2012) 153–161.
17 J. Bisquert, Theory of the impedance of electron diffusion and recombination in a thin layer, J. Phys. Chem. B 106 (2002) 325–333.
18 W. Ma, C. Yang, X. Gong, K. Lee, A.J. Heeger, Thermal stable, efficient polymer solar cells with nanoscale control of the interpenetrating network morphology, Adv. Funct. Mater. 15 (2005) 1617–1622.
19 A.D. Pasquier, H.E. Unalan, A. Kanwal, S. Miller, M. Chhowalla, Conducting and transparent single-wall carbon nanotube electrodes for polymer-fullerene solar cells, Appl. Phys. Lett. 87 (2005) 203511.